



# Structural, magnetic and magnetocaloric study of $\text{Ni}_{0.5}\text{Zn}_{0.5}\text{Fe}_2\text{O}_4$ spinel

B. Rabi<sup>1</sup> · A. Essoumhi<sup>2</sup> · M. Sajieddine<sup>1</sup> · J. M. Greneche<sup>3</sup> · E. K. Hlil<sup>4</sup> · A. Razouk<sup>1</sup> · M. A. Valente<sup>5</sup>

Received: 3 November 2019 / Accepted: 27 January 2020 / Published online: 11 February 2020  
© Springer-Verlag GmbH Germany, part of Springer Nature 2020

## Abstract

The objective of this work was to study the influence of annealing temperature on the structural changes and magnetic properties of the  $\text{Ni}_{0.5}\text{Zn}_{0.5}\text{Fe}_2\text{O}_4$  spinel-type nanoparticles. The nanomaterial was prepared by the chemical co-precipitation method and studied by thermal analysis (TG–DTA), X-ray diffraction (XRD), transmission electron microscopy (TEM), magnetic measurements and  $^{57}\text{Fe}$  Mössbauer spectrometry. XRD has revealed that the as-prepared sample shows poor crystallization with less defined diffraction lines. As the annealing temperature increases, the diffraction peaks become intense and well defined, reflecting perfect crystallization of the sample. The estimated crystallite size varies from 25 to 83 nm. TEM observations give information on the morphology and confirm the XRD results. To quantify the proportions of the iron atoms in the tetrahedral and octahedral sites, in-field Mössbauer spectrometry measurements were carried out at low temperature. Saturation magnetization ( $M_s$ ) and the average hyperfine magnetic field ( $\langle B_{\text{hf}} \rangle$ ) increase gradually with annealing temperature. For the sample annealed at 1000 °C, the magnetic entropy change  $|\Delta S_M^{\text{max}}|$  and relative cooling power, measured under field change of 2T, are 0.67 J kg<sup>-1</sup> K<sup>-1</sup> and 112.5 J kg<sup>-1</sup>, respectively.

**Keywords** Nickel–zinc ferrite nanoparticles · X-ray diffraction ·  $^{57}\text{Fe}$  Mössbauer spectrometry · Magnetic properties · Magnetocaloric effect

## 1 Introduction

The chemical and physical behaviors of spinel ferrites are highly dependent on composition, grain size and cation distribution in tetrahedral and octahedral sites. The reduction in the grain size of ferrites reveals new magnetic behaviors. In addition, the method and the conditions of synthesis of these nanomaterials as well as the annealing temperature

are critical factors that determine the microstructure and the physical properties. In this field, nanocrystalline magnetic spinel ferrite has attracted the attention of scientists and researchers because of its applications in diverse fields, such as data storage, hyperthermia, magnetic fluids, target drug delivery, magnetic refrigeration [1–7]. Various synthesis methods, such as co-precipitation [8], sol–gel [9], mechanochemical process [10], solid-state reaction [11], are commonly used by several authors to synthesize spinel ferrite nanoparticles.

Ni–Zn ferrites are soft magnetic ceramics having a spinel configuration where the oxygen anions are arranged in a face-centered cubic lattice. The distribution of divalent and trivalent cations between the tetrahedral and octahedral sites in this material can be expressed with formula  $(\text{Zn}_\lambda^{2+}\text{Fe}_{1-\lambda}^{3+})[\text{Ni}_{1-\lambda}^{2+}\text{Fe}_{1+\lambda}^{3+}]\text{O}_4$ , where  $\lambda$  is the degree of inversion. In this formula, the metallic cations  $(\text{Zn}_\lambda^{2+}\text{Fe}_{1-\lambda}^{3+})$  occupy the tetrahedral A sites and the metallic cations  $[\text{Ni}_{1-\lambda}^{2+}\text{Fe}_{1+\lambda}^{3+}]$  occupy the octahedral B sites [12]. For a normal ferrite such as  $\text{ZnFe}_2\text{O}_4$ ,  $\lambda$  is equal to 0 [13] and it is equal to 1 for an inverse spinel such as  $\text{NiFe}_2\text{O}_4$  [14], while for a mixed spinel structure, it is between 0 and 1 [15]. Thus, the

✉ M. Sajieddine  
sajieddinem@yahoo.fr

<sup>1</sup> Laboratoire de Physique des Matériaux, FST, Université Sultan Moulay Slimane, BP 523, 23000 Béni-Mellal, Maroc

<sup>2</sup> Laboratoire des Procédés Chimiques et Matériaux Appliqués, FP, Université Sultan Moulay Slimane, BP 523, 23000 Béni-Mellal, Maroc

<sup>3</sup> Institut des Molécules et Matériaux du Mans (IMMM), UMR CNRS 6283, 72085 Le Mans Cedex 9, France

<sup>4</sup> Institut Néel, CNRS - Université Grenoble Alpes, BP 166, 38042 Grenoble, France

<sup>5</sup> I3N and Physics Department, University of Aveiro, 3810-193 Aveiro, Portugal

physical properties of these nanomaterials strongly depend on the cation distribution and the magnetic interactions in A and B sites. As a result, to regulate the magnetic properties of these nanoferrites, it is necessary to control the cationic occupations at the interstices [16].

Spinel ferrite nanomaterials have also attracted considerable interest in their potential application as materials for the magnetic refrigeration [2, 3]. Although these nanomaterials present a slight change in entropy as compared to gadolinium [17] or other nanomaterials [18], they present several advantages make them promising for use in this field of application, such as their low production cost, their change ordering, their high magnetization and also their magnetocaloric effect (MCE) changed in the wide range of temperature. In addition, the ease of the synthesis method used and changes in chemical composition or adequate annealing makes possible the adjustment of the Curie temperature ( $T_C$ ), which allows expands the scope of the search for new refrigerant nanomaterials. Recently, El Maalam et al. [19] found that  $Zn_{1-x}Ni_xFe_2O_4$  ( $x=0.3$  and  $0.4$ ) synthesized by solid-state reaction had an important magnetic entropy, 1.41 and 1.45 J kg<sup>-1</sup> K<sup>-1</sup> in a field of 5T for  $x=0.3$  and  $0.4$ , respectively. They found that it had a large refrigerant capacity. Anwar et al. [3] reported a decrease in  $T_C$  from 845 to 302 K when Zn concentration increases from 0 to 0.7 in the same system, in which a maximum change in magnetic entropy at 2.5T ( $\sim 1.39$  J kg<sup>-1</sup> K<sup>-1</sup>) with relative cooling power of 161 J kg<sup>-1</sup> was observed for the  $Zn_{0.5}Ni_{0.5}Fe_2O_4$  sample.

In this work,  $Ni_{0.5}Zn_{0.5}Fe_2O_4$  nanoparticles were prepared using co-precipitation method and characterized by different techniques such as X-ray diffraction, transmission electron microscopy, <sup>57</sup>Fe Mössbauer spectrometry and vibrating sample magnetometer. We provide a detailed structural analysis in relation to magnetic and magnetocaloric properties.

## 2 Experimental procedure

The synthesis of the nickel–zinc ferrite powder was performed by the co-precipitation method using iron chloride hexahydrate ( $FeCl_3 \cdot 6H_2O$ ), nickel nitrate hexahydrate ( $Ni(NO_3)_2 \cdot 6H_2O$ ) and zinc nitrate hexahydrate ( $Zn(NO_3)_2 \cdot 6H_2O$ ). These precursors were weighed according to the formula of  $Ni_{0.5}Zn_{0.5}Fe_2O_4$  and then were dissolved in 100 ml of deionized water and stirred in a magnetic stirrer at 40 °C for 30 min. A NaOH solution of 1 M concentration was prepared and used as a precipitating agent. It was dipped into the above solution to have pH = 12. The resulting intermixture was stirred in a magnetic stirrer at 40 °C for 2 h. Then, the product was filtered using a vacuum pump and it was washed several times to remove the unwanted salt residues and other impurities. The precipitate was then dried at 80 °C for 12 h, and the obtained product was ground in

a mortar to have fine powder which is the raw sample. The dried powders were finally annealed in air for 2 h at different temperatures (600, 800, 900 and 1000 °C).

TG–DTA analyzer (LabSys EVO Setaram 1600) was used to investigate the thermal changes in the sample. TG–DTA plot shows that after 500 °C, there is no more loss of mass. The crystalline phase of the as-prepared and annealed materials was identified by powder X-ray diffractometer, D8 Advance, with  $CuK_\alpha$  radiation source ( $\lambda = 1.5406$  Å) at 40 kV and 40 mA in the range of  $15 \leq 2\theta \leq 75^\circ$  with step of  $0.02^\circ$ . We also observed the morphology and calculated the size of the particles from the micrograph obtained with the help of TEM (FEI Technai). The transmission Mössbauer spectra were recorded using a standard spectrometer with a <sup>57</sup>Co/Rh source, with an initial activity of 25 mCi, running in constant acceleration mode at room temperature and at 11 K under external magnetic field applied parallel to the direction of the incident  $\gamma$ -ray. To calculate the spectra and estimate the values of the hyperfine parameters, we have used the standard least square fitting program NORMOS [20]. To study the magnetocaloric effect (MCE) in the sample, magnetization measurements versus the temperature and the magnetic applied field were carried out using a BSI magnetometer equipped with three pairs of anti-Helmholtz coils developed at Louis Néel Laboratory in Grenoble.  $M(T)$  data were obtained in 200–800 K temperature range with an applied magnetic field of 0.05 T. Isothermal  $M(H)$  data were measured in the vicinity of Curie temperature in the range of 450–630 K by a step of 5 K and under an applied magnetic field varying from 1 to 5T.

## 3 Results and discussion

### 3.1 Structural properties

The X-ray diffraction patterns of the sample annealed at different temperatures are compared in Fig. 1: the shape of the patterns changes when the annealing temperature increases from 600 to 1000 °C. Indeed, the as-prepared sample shows poor crystallization with low and broadened peaks. As the annealing temperature increases, the structure evolves and the peaks become well defined. The diffraction peak analysis shows that in addition to the main phase of spinel ferrite Ni–Zn JCPDS card no. (08-0234), which is marked by Miller indices in Fig. 1, there is a secondary phase of  $\gamma$ - $Fe_2O_3$  JCPDS card no. (39-1346). The characteristic peaks of  $\gamma$ - $Fe_2O_3$  remain visible up to calcination temperature of 900 °C. For the sample annealed at 1000 °C, the diffraction peaks show the presence of a pure Ni–Zn spinel. Using DIFFRAC.EVA software, the diffraction peaks have been indexed with respect to the cubic spinel-type structure with space group Fd3m. It is also observed that the diffraction

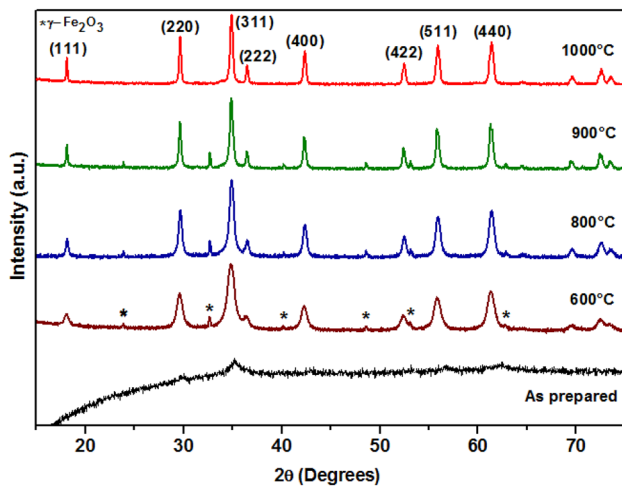


**Fig. 1** XRD patterns of the nanoparticles of Ni<sub>0.5</sub>Zn<sub>0.5</sub>Fe<sub>2</sub>O<sub>4</sub> annealed at different temperatures

peaks become narrower and sharper with increasing annealing temperature, indicating an increase in the crystallite size, which has been confirmed by the crystallite size calculation using the Scherrer equation at (311) peaks [8]:

$$D = 0.9 \frac{\lambda}{\Delta(2\theta) \cdot \cos \theta} \quad (1)$$

where  $D$  is the crystallite size in nm,  $\lambda$  is the wavelength of X-ray radiations,  $\theta$  is the Bragg's angle for diffraction peak and  $\Delta(2\theta)$  is the full width at half maximum for diffraction peak. The last two parameters are deduced from the spectra using X'Pert HighScore software. The evolution of the calculated crystallite sizes versus annealing temperature is depicted in Fig. 2. We can observe that the crystallite size increases gradually, from 25 to 83 nm, as the annealing temperature increases from 600 to 900 °C and becomes constant. According to Ayyappan [21], the growth of nanoparticles can be attributed to their coalescence by solid-state diffusion, where the system reduces its free energy by reducing the surface area of the nanoparticles.

The lattice parameter,  $a$ , can be written for a cubic system in the form [22]:

$$a = d_{hkl} \sqrt{h^2 + k^2 + l^2} \quad (2)$$

where  $d_{hkl}$  is the interplanar distance and  $h, k, l$  are the Miller indices. It's deduced from Bragg relation.

For an accurate calculation of the lattice constant, the lattice parameter was calculated for each peak of the XRD pattern and then the average of these values is determined. The estimated values of the lattice parameter,  $a$ , for each temperature are close. For the sample annealed at 1000 °C,  $a = 8.392 \text{ \AA}$  which is in good agreement with that found by other authors [23].

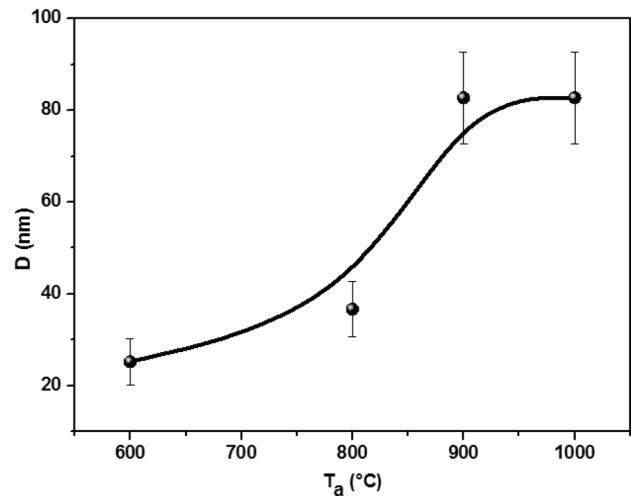


**Fig. 2** Variation of the crystallite size as a function of annealing temperature ( $T_a$ ). The solid line is a guide to the eyes

### 3.2 Morphology and chemical composition

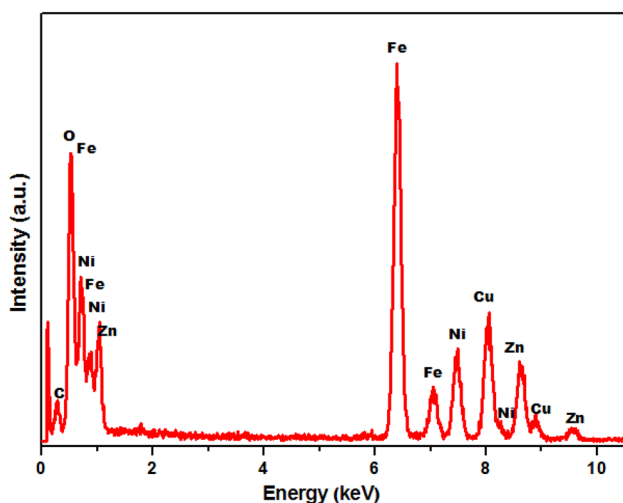
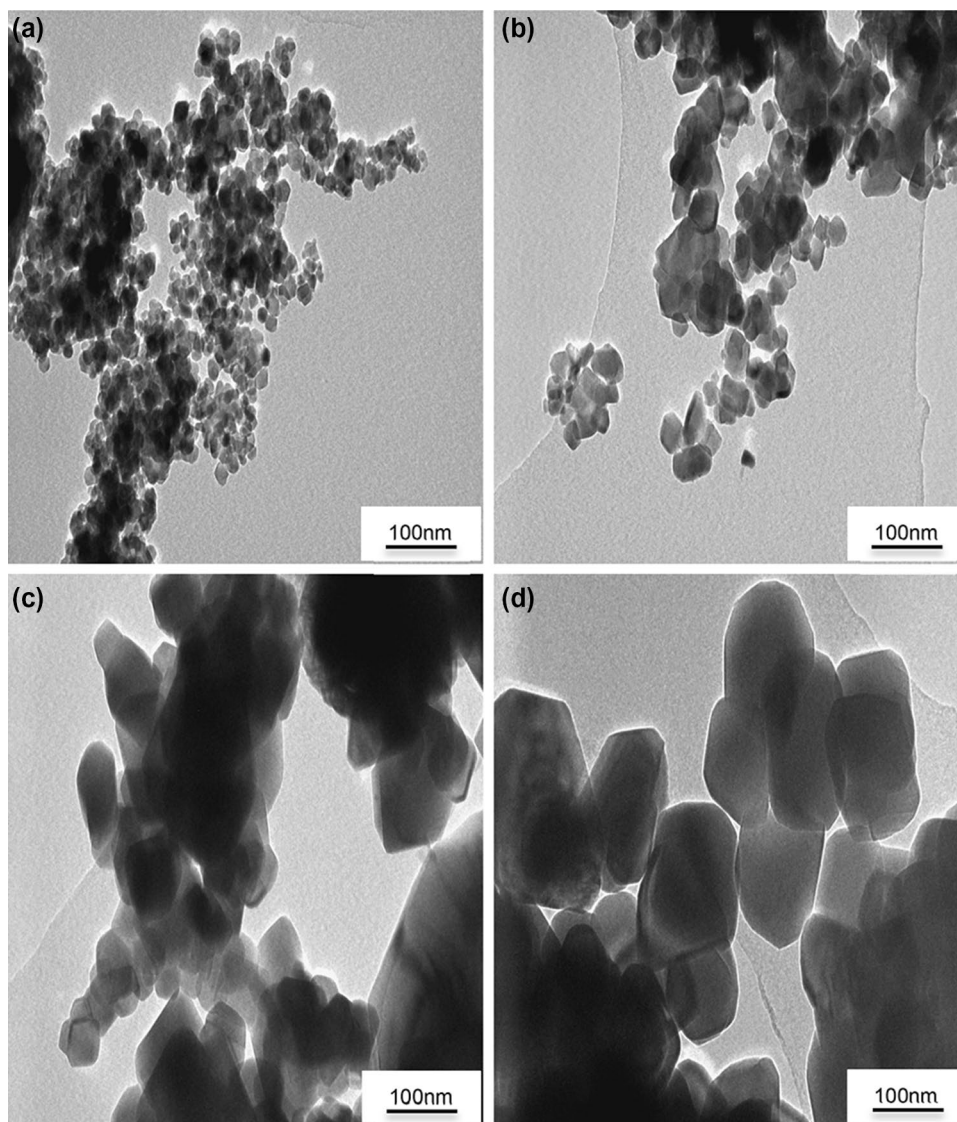
The morphology and microstructure of the samples were investigated by TEM micrographs illustrated in Fig. 3a–d. The images show that most of the observed nanoparticles have a spherical shape but some elongated nanoparticles are also present. As well, a low degree of agglomeration of nanoparticles is observed. Based on the TEM observations, it is seen that the size of the nanoparticles increases with the increase in the temperature. The estimated average nanoparticle size varies in the range 16–84 nm, which is in good agreement with XRD results.

Figure 4 shows energy-dispersive X-ray spectroscopy (EDX) elemental analysis of Ni<sub>0.5</sub>Zn<sub>0.5</sub>Fe<sub>2</sub>O<sub>4</sub> nanoparticles calcined at 1000 °C. The experimental chemical compositions of Ni, Zn, Fe and O estimated from EDX analysis are listed in Table 1. They are found to be similar to the expected stoichiometry of Ni<sub>0.5</sub>Zn<sub>0.5</sub>Fe<sub>2</sub>O<sub>4</sub>, while no impurities are detected in the sample. The observed peaks associated with carbon and copper, in the spectra, derived from the metallic grid on which we deposited the powders.

### 3.3 Mössbauer measurements

The confinement from bulk into nanostructured powder for Ni–Zn spinel ferrites is at the origin of the modification in the distribution of Fe<sup>3+</sup> ions between octahedral and tetrahedral sites. In order to study the cationic distribution and the iron coordination in Ni–Zn ferrite nanoparticles, <sup>57</sup>Fe Mössbauer spectrometry is one of the most appropriate techniques. Mössbauer spectra collected at room temperature of the samples annealed at different temperatures are shown in Fig. 5a. As the annealing temperature increases, the change

**Fig. 3** TEM images, for a scale of 100 nm, of the annealed samples at 600 (a), 800 (b), 900 (c), 1000 °C (d)



**Fig. 4** EDX spectra of  $\text{Ni}_{0.5}\text{Zn}_{0.5}\text{Fe}_2\text{O}_4$  sample annealed at 1000 °C

**Table 1** Weight and atomic percentages for  $\text{Ni}_{0.5}\text{Zn}_{0.5}\text{Fe}_2\text{O}_4$

Element	Weight (%)	Atomic percentage
O	19.7	47.2
Fe	51.7	35.3
Ni	13.4	8.7
Zn	15.2	8.8

of the hyperfine structure is attributed to the progressive increase in the blocked magnetic states at the expense of the decrease in the superparamagnetic states. The spectrum recorded using a low velocity range for the as-prepared (Fig. 5b) consists of a quadrupole doublet with broadened and asymmetrical lines due to dynamic and surface effects:

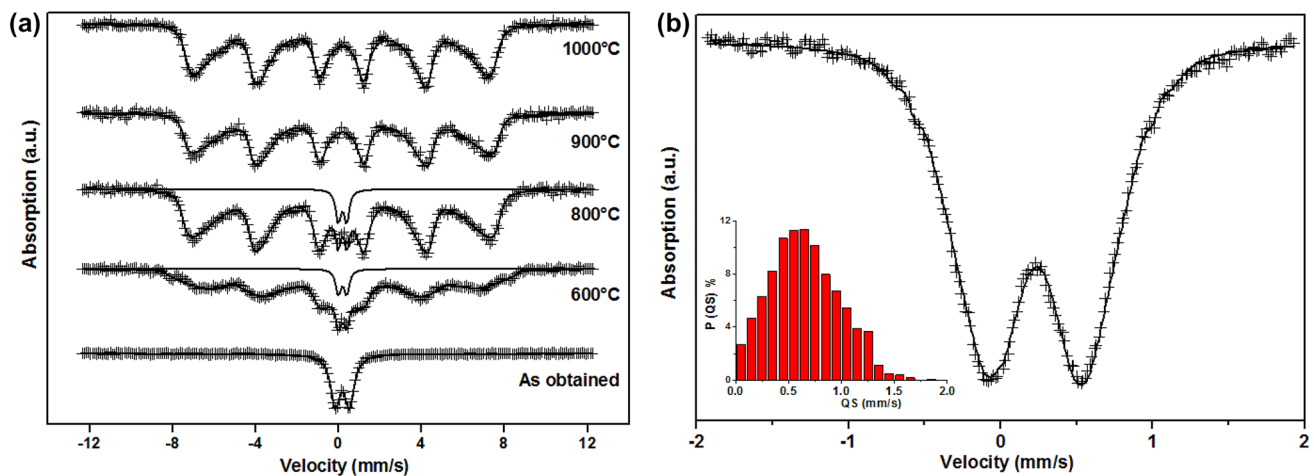


**Fig. 5** Room Mössbauer spectra of  $\text{Ni}_{0.5}\text{Zn}_{0.5}\text{Fe}_2\text{O}_4$  samples for different annealing temperatures (a) and Mössbauer spectrum related to the as obtained sample measured using the low velocity (b). The

points represented by (+) correspond to the experimental spectra and the solid line represents the fit

it can be well described by means of a discrete distribution of quadrupolar splitting (Fig. 5b) correlated linearly with that of isomer shift, allowing the small asymmetry to be well reproduced. This is consistent with the presence of  $\text{Fe}^{3+}$  species located in both tetrahedral and octahedral units. In addition, the value of  $q = \langle QS^2 \rangle / \langle QS \rangle^2 = 1.29$  is fairly consistent with that expected in the case of an amorphous structure (1.273 [24]). This completely corroborates the conclusion established from X-ray diffraction. It is important to note that the present quadrupolar doublet is not due to the presence of superparamagnetic relaxation phenomena, as the particles are too large [25].

As illustrated in Fig. 5a, the spectra of powders annealed at 600 and 800 °C result from the superposition of a magnetic sextet with broadened and non-Lorentzian lines and a quadrupolar feature in the center. These spectra can be well modeled with a superposition of two components: (1) a hyperfine field distribution attributed to some atomic Fe, Ni, and Zn disorder in the vicinity of the tetrahedral and octahedral  $\text{Fe}^{3+}$  probes, and (2) a quadrupole doublet due to some remaining amorphous domains. To adjust correctly the spectrum related to sample annealed at 600 °C, we added to both components two sextets whose total area does not exceed 7% of the total spectrum area. The calculated hyperfine parameters ( $B_{\text{hf}} = 50\text{T}$ ,  $\delta = 0.3 \text{ mm s}^{-1}$ ) and ( $B_{\text{hf}} = 51\text{T}$ ,  $\delta = 0.42 \text{ mm s}^{-1}$ ) are associated with A and B sites [26], respectively, of  $\gamma\text{-Fe}_2\text{O}_3$  impurity phase observed by XRD. For the spectrum recorded at 800 °C, the impurity phase of  $\gamma\text{-Fe}_2\text{O}_3$  is not well observed, and it was neglected.

However, the spectra collected on powders annealed at 900 and 1000 °C consist only of a magnetic broad component which can be well described with a distribution of hyperfine field. Such a feature indicates the formation of

a non-well ordered  $\text{Ni}_{0.5}\text{Zn}_{0.5}\text{Fe}_2\text{O}_4$  spinel phase resulting from the contribution of the thermal energy to redistribute cationic in their favorite sites. The values of the hyperfine parameters characteristic of these spectra are summarized in Table 2. The calculated values of isomer shift ranged between 0.30 and 0.35  $\text{mm s}^{-1}$  are consistent with the presence of high spin state  $\text{Fe}^{3+}$ . As depicted in Fig. 6, the average hyperfine field  $\langle B_{\text{hf}} \rangle$  increases with the particles size but remains smaller than the value estimated for the bulk material,  $B_{\text{hf}}^{\text{Bulk}} = 51.4\text{T}$  [27]. In addition, the increase in  $\langle B_{\text{hf}} \rangle$  with annealing temperature results from the progressive structural transformation from the amorphous to the crystalline state, thus promoting an increase in the magnetic order in each sublattice. For its part, the relative area of the doublet decreases and disappears completely at an annealing temperature of 800 °C when the crystallization of Ni–Zn ferrite is well improved, as can be seen on the XRD patterns.

Conventional Mössbauer spectrometry remains inappropriate to discriminate contributions of both A and B sites to the total spectrum in the case of ferrites and to estimate their relative proportions due to a lack of resolution of the hyperfine structure. However, the use of Mössbauer spectrometry under magnetic field is necessary to arrange the magnetic moments and then split the two Mössbauer components corresponding to A and B sites (see details in [28] and references therein). Figure 7 shows the Mössbauer spectrum of the  $\text{Ni}_{0.5}\text{Zn}_{0.5}\text{Fe}_2\text{O}_4$  sample annealed at 1000 °C, collected at 11 K under an external magnetic field of 8T applied parallel to the  $\gamma$ -beam: one observes clearly two well resolved sextets with low intensity intermediate lines. The refined values of hyperfine parameters are listed in Table 3. In this case,  $B_{\text{eff}}$  corresponds to the field at  $^{57}\text{Fe}$  measured under the external magnetic field  $B_{\text{app}}$ . By comparing the values of

**Table 2** Refined values of Mössbauer hyperfine parameters at 300 K for different annealing temperatures ( $T_a$ ): *HFD* (hyperfine field distribution), *QD* (quadrupole doublet),  $B_{\text{hf}}$  (hyperfine field),  $\delta$  (isomer shift),  $\Delta EQ$  (quadrupole separation) and  $2\epsilon$  (quadrupole shift)

$T_a$ (°C)	Component	Relative area $\pm 1$ (%)	$\langle B_{\text{hf}} \rangle \pm 1.0$ (T)	$\langle \delta \rangle \pm 0.02$ (mm s <sup>-1</sup> )	$\langle \Delta EQ \rangle$ or $\langle 2\epsilon \rangle \pm 0.02$ (mm s <sup>-1</sup> )
1000	HFD	100	36.2	0.46	0.00
900	HFD	100	35.8	0.38	0.00
800	HFD	95	33.9	0.34	0.00
	QD	5	–	0.33	0.40
600	HFD	87.4	29.0	0.32	0.00
	QD	5.6	–	0.34	0.40
	Site A	2.7	50.0	0.30	0.00
	Site B	4.3	51.0	0.42	0.00
As-prepared	QD	100	–	0.34	0.67

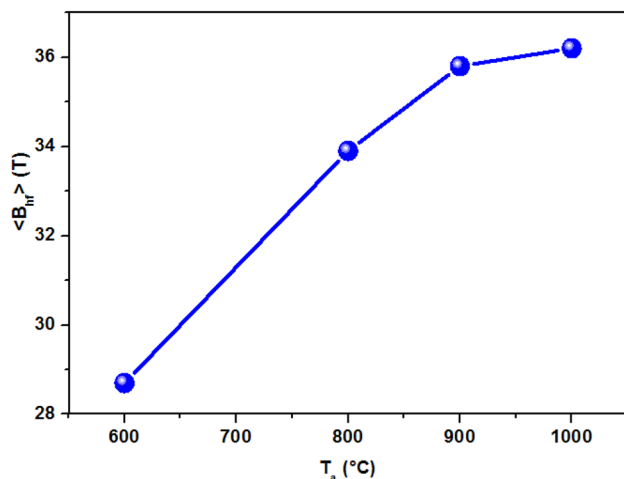


**Fig. 6** Evolution of the average hyperfine field  $\langle B_{\text{hf}} \rangle$  versus annealing temperature ( $T_a$ ). The solid line is a guide to the eyes

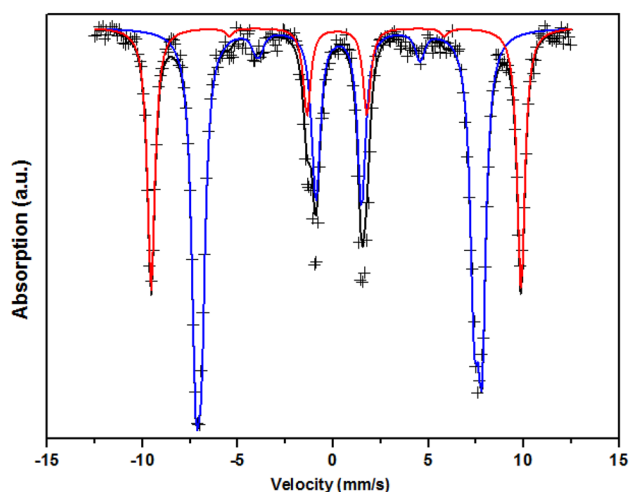


**Fig. 7** Mössbauer spectra of  $\text{Ni}_{0.5}\text{Zn}_{0.5}\text{Fe}_2\text{O}_4$  measured at 11 K under an external magnetic field of 8T. The points represented by (+) correspond to the experimental spectra, and the solid line represents the fit

**Table 3** Refined values of Mössbauer hyperfine parameters at 11 K under an external magnetic field of 8T:  $B_{\text{eff}}$  (effective field),  $B_{\text{hf}}$  (hyperfine field),  $\delta$  (isomer shift),  $2\epsilon$  (quadrupole shift) and  $\theta$  (canting angle)

	$B_{\text{eff}}$ (T)	$B_{\text{hf}}$ (T)	$\delta$ (mm s <sup>-1</sup> )	$2\epsilon$ (mm s <sup>-1</sup> )	$\theta$ (°)
A site	$60 \pm 0.5$	$52.2 \pm 0.5$	$0.38 \pm 0.01$	$-0.04 \pm 0.02$	$12 \pm 5$
B site	$44.2 \pm 0.5$		$0.49 \pm 0.01$	$-0.07 \pm 0.02$	$18 \pm 5$
	$46.4 \pm 0.5$		$0.49 \pm 0.01$	$0.02 \pm 0.02$	$16 \pm 5$
	$\langle 45.3 \rangle \pm 0.5$	$\langle 53.0 \rangle \pm 0.5$	$\langle 0.49 \rangle \pm 0.01$	$\langle -0.02 \rangle \pm 0.02$	$\langle 17 \rangle \pm 5$

isomer shift, the sextet with  $B_{\text{eff}} = 60\text{T}$  and  $\delta = 0.38\text{ mm s}^{-1}$  is clearly attributed to iron atoms in A sites while the other one ( $B_{\text{eff}} = 45.3\text{T}$  and  $\delta = 0.49\text{ mm s}^{-1}$ ) is assigned to the B sites with relative proportions equal to 31 and 69%, respectively. So, the lowest  $B_{\text{eff}}$  value corresponds to the iron magnetic moments aligned to external field direction, while the highest  $B_{\text{eff}}$  value corresponds to other iron moments aligned in the opposite direction of the external field. One can conclude that the hyperfine fields are opposite to magnetic moments of iron, resulting from the large and negative value of the contact term contribution, as expected. The values of the hyperfine magnetic fields  $B_{\text{hf}}$  can be calculated from the relation:

$$B_{\text{hf}}^2 = B_{\text{eff}}^2 + B_{\text{app}}^2 - 2 \cdot B_{\text{eff}} B_{\text{app}} \cdot \cos \theta \quad (3)$$

where  $\theta$  is the canting angle given by the expression:

$$\theta = \arccos \left( \sqrt{\frac{4-x}{4+x}} \right) \quad (4)$$

where  $x$  is the intensity of the intermediate lines 2 and 5. Thus, the estimated values of hyperfine fields  $B_{\text{hf}}$  are 52.2 and 53T for A and B sites, respectively.

If we consider that  $I_A$  and  $I_B$  represent the intensity of subspectral A and B, the degree of cation inversion  $\lambda$  of spinel can be calculated using the hyperfine parameters

deduced from the fit of the spectrum measured under external field, according to the relation:

$$\frac{I_A}{I_B} = \frac{f_A}{f_B} \cdot \frac{\lambda}{2 - \lambda} \quad (5)$$

$I_A/I_B$  represents the Fe<sup>3+</sup> ion fraction ratio which is proportional to the area ratio of tetrahedral and octahedral sites,  $f_A/f_B$  is the ratio of the recoilless fractions equivalent to about 0.94 at room temperature but tends to 1 at low temperature [29, 30] and  $\lambda$  is the fraction of Fe<sup>3+</sup> in A site. It follows that the estimated value of  $\lambda$  is 0.62, which indicate that some of Zn<sup>2+</sup> moves from A to B site. Thus, the cation distribution can be expressed as (Zn<sub>0.38</sub><sup>2+</sup> Fe<sub>0.62</sub><sup>3+</sup>) [Zn<sub>0.12</sub><sup>2+</sup> Ni<sub>0.50</sub><sup>2+</sup> Fe<sub>1.38</sub><sup>2+</sup>]O<sub>4</sub>. The present result is closely consistent with those reported by Jadhav et al. [31] and Gabal et al. [32], respectively.

### 3.4 Magnetization measurements

The magnetic behavior of spinel ferrites depends on several factors such as the synthesis technique, the distribution of cations into tetrahedral and octahedral sites and the size of the crystalline grain in the case of confined structures [33]. Typical plots of  $M-H$  of Ni<sub>0.5</sub>Zn<sub>0.5</sub>Fe<sub>2</sub>O<sub>4</sub> nanoparticles, annealed at 1000 °C, measured at 5 and 300 K are depicted in Fig. 8. As can be seen, the  $M-H$  plots show that the samples exhibit a typical ferrimagnetic behavior. The saturation is reached by applying a magnetic field of 1.25 and 0.86T, respectively.

The evolution of the saturation magnetization ( $M_s$ ) obtained from the hysteresis loops is presented in Fig. 9. It is observed that  $M_s$  increases significantly with particle size. The increase in  $M_s$  can be explained by the interactions between ions occupying A and B sites [34]. So, at the

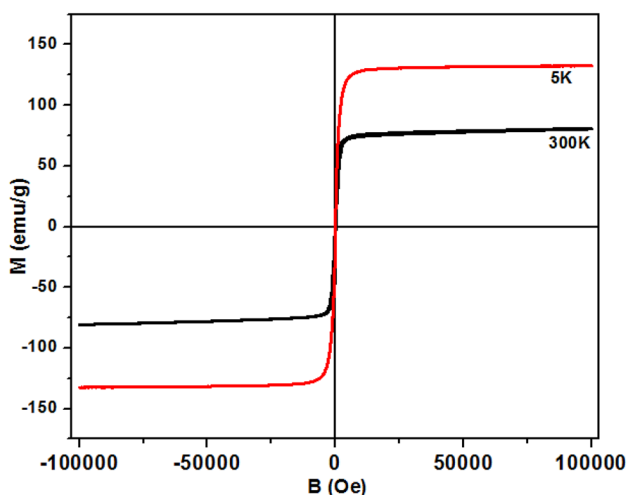


**Fig. 8** Magnetization versus applied field of Ni<sub>0.5</sub>Zn<sub>0.5</sub>Fe<sub>2</sub>O<sub>4</sub> annealed at 1000 °C

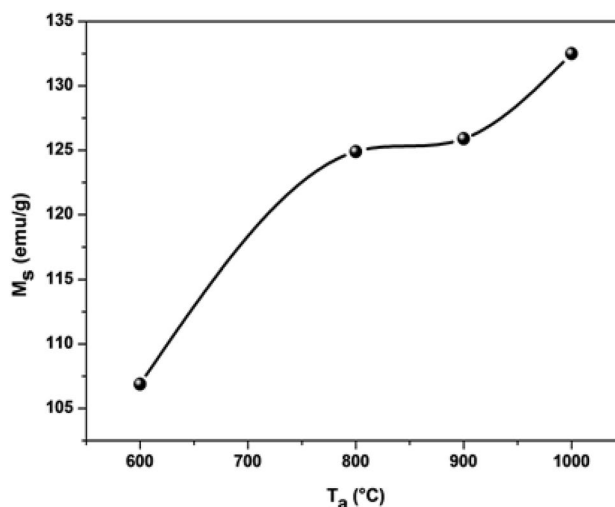


**Fig. 9** Evolution of  $M_s$ , at 5 K, with annealing temperature ( $T_a$ ). The solid line is a guide to the eyes

surface of nanoparticles, a dead layer is formed due to the uncompensated exchange interactions. For small particle size, the ratio of surface area to volume increases, so the dead layer becomes more dominant than the volume which leads to a decrease in A–B interaction and therefore the magnetization ( $M_s$ ) decrease. The opposite case is seen as the particle sizes increase [35]. For the sample annealed at 1000 °C,  $M_s$  is above 132 emu g<sup>-1</sup>. The obtained values of  $M_s$  are more important than those obtained for bulk Nickel and Zinc ferrites [36, 37]. According to Berkowitz et al. [38],  $M_s$  varies with particles size  $D$  like  $M_s = M_s^B \cdot \left(1 - \frac{C}{D}\right)$  where  $M_s^B$  is the saturation magnetization of the bulk ferrite and  $C$  is a constant. The values of  $M_s^B$  and  $C$  are obtained by plotting  $M_s$  versus  $D$ . The slope gives the value of  $M_s^B$ , and the intercept gives that of  $C$ . Note that  $C = 6t$ , where  $t$  is the thickness of the magnetic dead layer located at the surface of the nanoparticles. The presence of the nonmagnetic layer is related to the existence of canting of particle surface spins. We have estimated the value of  $t$  to 0.74 nm, which is in good agreement with those reported by others authors in NiZnFe<sub>2</sub>O<sub>4</sub> [39], MnFe<sub>2</sub>O<sub>4</sub> [40] and LiFe<sub>2</sub>O<sub>4</sub> [38].

### 3.5 Magnetocaloric effect investigation

In this part, we limit the study to the sample annealed at 1000 °C which has a pure spinel structure and a highest saturation magnetization values ( $M_s = 132$  emu g<sup>-1</sup> at 5 K). To study the magnetocaloric effect (MCE), first the temperature dependence of field-cooled (FC) magnetization under an applied field of 0.05T was measured, as can be seen in Fig. 10. From this curve, the sample exhibits a clear transition from ferrimagnetic (FM) to paramagnetic (PM) state

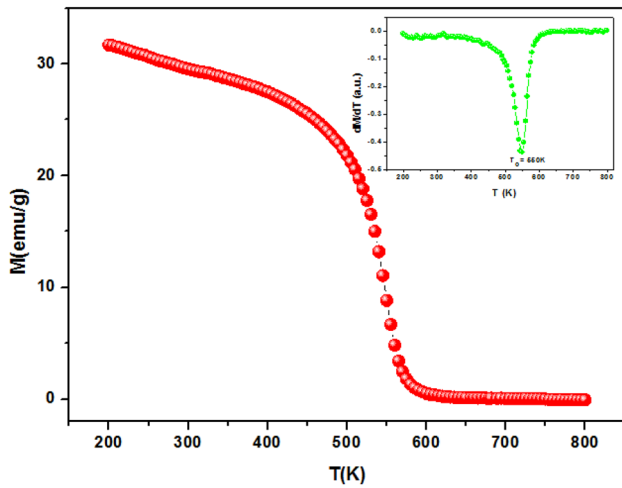


**Fig. 10** Magnetization of  $\text{Ni}_{0.5}\text{Zn}_{0.5}\text{Fe}_2\text{O}_4$  as a function of the temperature at magnetic field of 0.05T. The insert of plot represents  $dM/dT$  versus  $T$  for  $\text{Ni}_{0.5}\text{Zn}_{0.5}\text{Fe}_2\text{O}_4$  sample

with increasing temperature. Curie temperature  $T_C$  was confirmed from the derivative of magnetization  $dM/dT$  versus  $T$  curve which is shown in the inset of Fig. 10. The observed minimum at 550 K corresponds to  $T_C$ . At this temperature, the magnetic entropy presents a large change. To investigate the MCE of the sample at different temperature regions, we measured isothermal variation of the magnetization  $M$  versus the applied magnetic field  $\mu_0 H$  at different temperatures  $T$ , with step of 5 K (Fig. 11). As we can see, the isotherms below 550 K differ from those measured at high temperature. Thus, the isotherms beyond 550 K show visible curvatures but no tendency to saturation has been observed. From  $M(\mu_0 H)$  curves, we plotted the Arrott curves  $M^2$  versus  $\mu_0 H/M$ , as shown in Fig. 12. According to Banerjee criteria [41], a positive slope of  $M^2$  versus  $\mu_0 H/M$  is the signature of

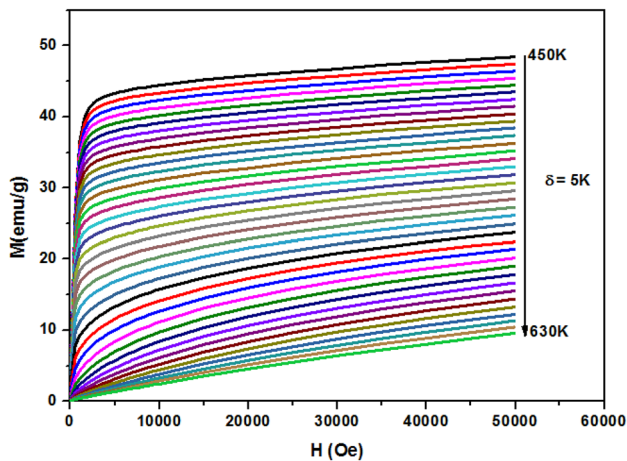


**Fig. 11** Isothermal magnetization curves  $M(H)$  of  $\text{Ni}_{0.5}\text{Zn}_{0.5}\text{Fe}_2\text{O}_4$  at different temperatures

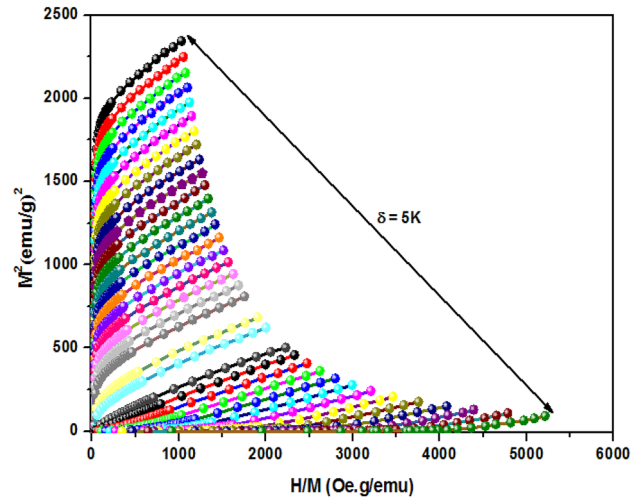


**Fig. 12** Arrott plot of  $\text{Ni}_{0.5}\text{Zn}_{0.5}\text{Fe}_2\text{O}_4$  sample annealed at 1000 °C

the existence of a second-order magnetic phase transition, on the other hand a negative slope indicates the existence of first-order one. For this sample, the magnetic phase transition is of second order.

Materials with a first-order transition are characterized by a strong variation in magnetic entropy but present a small temperature range  $\delta T_{FWHM}$ . Giant magnetocaloric effects are found in this family of materials and in this situation, the transition is irreversible and the Maxwell relation cannot be used because its non-equilibrium application can lead to overestimations of  $\Delta S_M$ . On the other hand, materials with a second-order transition have a small variation in magnetic entropy change extending over a wide temperature range  $\delta T_{FWHM}$ . For these materials, the Maxwell method is generally applied to determine the variation of the magnetic entropy change ( $-\Delta S_M$ ) caused by the application of the applied field ( $\mu_0 H$ ) [42, 43]. So, Maxwell relation is given by using the following expression [44]:

$$\Delta S_M = \int_0^H \left( \frac{\partial M}{\partial T} \right)_H \cdot dH \tag{6}$$

$$\Delta S_M = \sum_i \frac{M_i - M_{i+1}}{T_i - T_{i+1}} \Delta H_i$$

where  $M_i$  and  $M_{i+1}$  are the experimental values of the magnetization at  $T_i$  and  $T_{i+1}$  under a magnetic field  $H_i$ , respectively. The values of  $M$ ,  $T$  and  $H$  are determined from the isothermal curves of magnetization  $M(\mu_0 H)$ .

Figure 13 illustrates the magnetic entropy change for sample heat treated at 1000 °C as a function of temperature at different fields ( $\Delta H = 1, 2, 3, 4$  and 5T).  $-\Delta S_M$  takes a maximum around  $T_C$ ; as well, it increases with increasing applied magnetic field. At the 2T magnetic



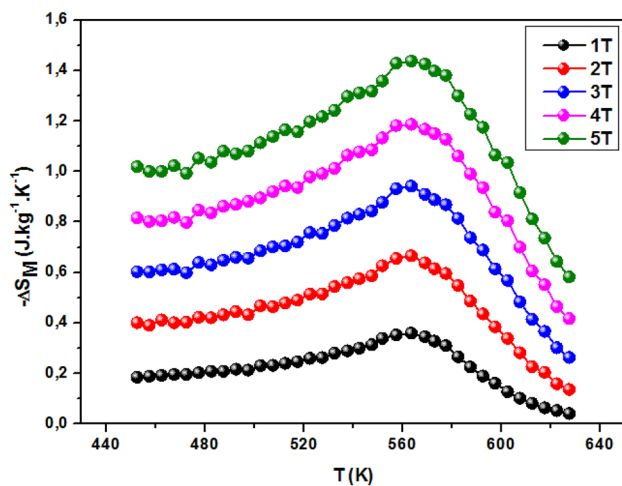


**Fig. 13** Temperature dependence of magnetic entropy change under different magnetic fields for Ni<sub>0.5</sub>Zn<sub>0.5</sub>Fe<sub>2</sub>O<sub>4</sub>

field, a value of the maximum magnetic entropy change ( $-\Delta S_M^{\max}$ ) of  $0.67 \text{ J kg}^{-1} \text{ K}^{-1}$  is observed. This value is no less important than that found in the literature [3, 19]. To evaluate the magnetic refrigeration quality of the sample, we determine the relative cooling power (RCP) using the following relation [45]:

$$\text{RCP} = -\Delta S_M^{\max} \times \delta T_{\text{FWHM}} \quad (7)$$

where  $\delta T_{\text{FWHM}}$  is the full width at half maximum of the magnetic entropy change curve  $-\Delta S_M(T)$ . The found values of  $T_C$ ,  $-\Delta S_M$  and RCP are compared to available data (Table 4). Also, we can note that the calculated RCP is comparable to that of some perovskite and spinel materials [46, 47]. The magnetocaloric parameters ( $-\Delta S_M$  and RCP) for our sample are close to that of Ni<sub>0.5</sub>Zn<sub>0.5</sub>Fe<sub>2</sub>O<sub>4</sub> synthesized by solid-state reaction [3] for which the Curie temperature is 481 K, ( $0.67 \text{ J kg}^{-1} \text{ K}^{-1}$  vs.  $1.04 \text{ J kg}^{-1} \text{ K}^{-1}$ ) and ( $112.5 \text{ J kg}^{-1}$  vs.  $138 \text{ J kg}^{-1}$ ), respectively. The noted difference is attributed to the grain size, which is higher in solid-state reaction. Based on the above results, we consider that our sample possesses rather good magnetocaloric properties at high temperatures.

## 4 Conclusion

In this work, we have studied the effect of the annealing temperature (600–1000 °C) on the structural and magnetic properties of Ni<sub>0.5</sub>Zn<sub>0.5</sub>Fe<sub>2</sub>O<sub>4</sub> compound synthesized by co-precipitation method. According to the XRD results, for annealing temperature equal to 1000 °C, the sample crystallizes in Fd3m cubic system and no impurities have been detected. The crystallite size estimated by X-ray diffraction increases from 25 to 83 nm with increasing the annealing temperature from 600 up to 1000 °C. On the other hand, the observations as well as the EDX carried out by TEM confirm the results obtained by X-ray diffraction. Room temperature Mössbauer spectra show clearly the effect of the annealing temperature. They change from a paramagnetic doublet for the as-prepared sample to a purely magnetic broad peak component for that annealed at 1000 °C. The average hyperfine magnetic field increases with increasing crystallite size. Also, Mössbauer spectrometry recorded at 11 K under an external magnetic field has been used in order to evaluate the proportions of the Fe<sup>3+</sup> species located in A and B sites and so to estimate the cationic inversion degree. Magnetocaloric measurements evince that our sample, under a magnetic applied field change of 2T, presents an important relative cooling power (RCP),  $112.5 \text{ J kg}^{-1}$ , at Curie temperature of 550 K. This sample shows the highest saturation magnetization values and this can be beneficial for magnetocaloric applications; work is in progress to bring  $T_C$  close to room temperature and also to improve its physical properties by doping it with other elements.

**Table 4** Curie temperature  $T_C$ , magnetic entropy change  $-\Delta S_M$  and relative cooling power RCP

	$\mu_0 H$ (T)	$T_C$ (K)	$-\Delta S_M$ ( $\text{J kg}^{-1} \text{ K}^{-1}$ )	RCP ( $\text{J kg}^{-1}$ )	References
Ni <sub>0.5</sub> Zn <sub>0.5</sub> Fe <sub>2</sub> O <sub>4</sub>	2	550	0.67	112.5	This work
Ni <sub>0.5</sub> Zn <sub>0.5</sub> Fe <sub>2</sub> O <sub>4</sub>	2	481	1.04	138.0	[3]
La <sub>0.8</sub> Na <sub>0.15</sub> K <sub>0.05</sub> MnO <sub>3</sub>	2	330	2.09	107.5	[40]
Pr <sub>0.6</sub> Sr <sub>0.35</sub> K <sub>0.05</sub> MnO <sub>3</sub>	2	303	3.09	95.6	[41]

## References

1. E. Veena Gopalan, I.A. Al-Omari, K.A. Malini, P.A. Joy, D.S. Kumar, Y. Yoshida, M.R. Anantharaman, Impact of zinc substitution on the structural and magnetic properties of chemically derived nanosized manganese zinc mixed ferrites. *J. Magn. Magn. Mater.* **321**, 1092–1099 (2009)
2. S.S. Jadhav, S.E. Shirsath, S.M. Patange, K.M. Jadhav, Effect of Zn substitution on magnetic properties of nanocrystalline cobalt ferrite. *J. Appl. Phys.* **108**, 93920 (2010)
3. M.S. Anwar, F. Ahmed, B.H. Koo, Enhanced relative cooling power of  $\text{Ni}_{1-x}\text{Zn}_x\text{Fe}_2\text{O}_4$  ( $0.0 \leq x \leq 0.7$ ) ferrites. *Acta Mater.* **71**, 100–107 (2014)
4. M.E. McHenry, D.E. Laughlin, Nano-scale materials development for future magnetic applications. *Acta Mater.* **48**, 223–238 (2000)
5. G.F. Goya, H.R. Rechenberg, J.Z. Jiang, Structural and magnetic properties of ball milled copper ferrite. *J. Appl. Phys.* **84**, 1101 (1998)
6. Z.X. Yue, J. Zhou, X.H. Wang, Z.L. Gui, L.T. Li, Low-temperature sintered Mg–Zn–Cu ferrite prepared by auto-combustion of nitrate–citrate gel. *J. Mater. Sci. Lett.* **20**, 1327–1329 (2001)
7. N. Ponpandian, P. Balaya, A. Narayanasamy, Electrical conductivity and dielectric behaviour of nanocrystalline  $\text{NiFe}_2\text{O}_4$  spinel. *J. Phys.: Condens. Matter.* **14**, 3221–3237 (2002)
8. D.G. Chen, X.G. Tang, J.B. Wu, W. Zhang, Q.X. Liu, Y.P. Jiang, Effect of grain size on the magnetic properties of superparamagnetic  $\text{Ni}_{0.5}\text{Zn}_{0.5}\text{Fe}_2\text{O}_4$  nanoparticles by co-precipitation process. *J. Magn. Magn. Mater.* **323**, 1717–1721 (2011)
9. R.C. Pedroza, S.W. da Silva, M.A.G. Soler, P.P.C. Saratto, D.R. Rezende, P.C. Morais, Raman study of nanoparticle-template interaction in a  $\text{CoFe}_2\text{O}_4/\text{SiO}_2$ -based nanocomposite prepared by sol–gel method. *J. Magn. Magn. Mater.* **289**, 139–141 (2005)
10. H. Yang, X.C. Zhang, W.Q. Ao, G.Z. Qiu, Formation of  $\text{NiFe}_2\text{O}_4$  nanoparticles by mechanochemical reaction. *Mater. Res. Bull.* **39**, 833–837 (2004)
11. M. Ajmal, A. Maqsood, Influence of zinc substitution on structural and electrical properties of  $\text{Ni}_{1-x}\text{Zn}_x\text{Fe}_2\text{O}_4$  ferrites. *Mater. Sci. Eng. B* **139**, 164–170 (2007)
12. J.M. Daniels, A. Rosenwaig, Mössbauer study of the Ni–Zn ferrite system. *Rev. Can. Phys.* **48**(4), 381–396 (1970)
13. H. Yang, X.C. Zhang, C.H. Huang, W.G. Yang, G.Z. Qiu, Synthesis of  $\text{ZnFe}_2\text{O}_4$  nanocrystallites by mechanochemical reaction. *J. Phys. Chem. Solids* **65**, 1329–1332 (2004)
14. J.H. Liu, L. Wang, F.S. Li, Magnetic properties and Mössbauer studies of nanosized  $\text{NiFe}_2\text{O}_4$  particles. *J. Mater. Sci.* **40**, 2573–2575 (2005)
15. I.S. Lyubutin, C.R. Lin, S.S. Starchikov, A.O. Baskakov, N.E. Gervits, K.O. Funtov, Y.T. Tseng, W.J. Lee, K.Y. Shih, J.S. Lee, Structural, magnetic, and electronic properties of mixed spinel  $\text{NiFe}_{2-x}\text{Cr}_x\text{O}_4$  nanoparticles synthesized by chemical combustion. *Inorg. Chem.* **56**, 12469–12475 (2017)
16. G. Salazar-Alvarez, R.T. Olsson Jordi Sort, W.A.A. Macedo, J.D. Ardisson, M. Dolores Baro, U.W. Gedde, J. Noguez, Enhanced coercivity in co-rich near-stoichiometric  $\text{Co}_x\text{Fe}_{3-x}\text{O}_{4+\delta}$  nanoparticles prepared in large batches. *Chem. Mater.* **19**, 4957–4963 (2007)
17. S.M. Benford, G.V. Brown,  $T$ – $S$  diagram for gadolinium near the Curie temperature. *J. Appl. Phys.* **52**, 2110 (1981)
18. E. Oumezzine, S. Hcini, M. Baazaoui, E.K. Hlil, M. Oumezzine, Structural, magnetic and magnetocaloric properties of  $\text{Zn}_{0.6-x}\text{Ni}_x\text{Cu}_{0.4}\text{Fe}_2\text{O}_4$  ferrite nanoparticles prepared by Pechini sol–gel method. *Powder Technol.* **278**, 189–195 (2015)
19. K. El Maalam, L. Fkhar, M. Hamedoun, A. Mahmoud, F. Boschini, E.K. Hlil, A. Benyoussef, O. Mounkachi, Magnetocaloric properties of zinc–nickel ferrites around room temperature. *J. Supercond. Nov. Magn.* **30**(7), 1943–1947 (2017)
20. R.A. Brand, Normos Mössbauer fitting program. *Nucl. Instr. Methods B* **28**, 398–416 (1987)
21. S. Ayyappan, G. Gnanaprakash, G. Paneerselvam, M.P. Antony, Effect of surfactant monolayer on reduction of  $\text{Fe}_3\text{O}_4$  nanoparticles under vacuum. *J. Phys. Chem.* **112C**, 18376–18383 (2008)
22. S.S. Kumbhar, M.A. Mahadik, V.S. Mohite, K.Y. Rajpure, J.H. Kim, A.V. Moholkar, C.H. Bhosale, Structural, dielectric and magnetic properties of Ni substituted zinc ferrite. *J. Magn. Magn. Mater.* **363**, 114–120 (2014)
23. A.S. Albuquerque, J.D. Ardisson, W.A.A. Macedo, M.C.M. Alves, Nanosized powders of NiZn ferrite: synthesis, structure, and magnetism. *J. Appl. Phys.* **87**, 4352 (2000)
24. M.E. Lopez-Herrera, J.M. Greneche, F. Varret, Analysis of the Mössbauer quadrupole spectra of some amorphous fluorides. *Phys. Rev. B* **28**, 4944–4948 (1983)
25. J.J. Thomas, A.B. Shinde, P.S.R. Krishna, N. Kalarikkal, Cation distribution and micro level magnetic alignments in the nanosized nickel zinc ferrite. *J. Alloys Compd.* **546**, 77–83 (2013)
26. J.A. Ramos Guivar, E.A. Sanches, F. Bruns, E. Sadrollahi, M.A. Morales, E.O. López, F.J. Litterst, Vacancy ordered  $\gamma\text{-Fe}_2\text{O}_3$  nanoparticles functionalized with nanohydroxyapatite: XRD, FTIR, TEM, XPS and Mössbauer studies. *Appl. Surf. Sci.* **389**, 721–734 (2016)
27. V. Sreeja, S. Vijayanand, S. Deka, P.A. Joy, Magnetic and Mössbauer spectroscopic studies of NiZn ferrite nanoparticles synthesized by a combustion method. *Hyperfine Interact.* **183**(99), 271–279 (2008)
28. J.M. Greneche, *Mössbauer Spectroscopy*, ed. by Y. Yoshida, G. Langouche (Springer, Berlin, 2013), pp. 187–241
29. V. Šepelák, D. Baabe, D. Mienert, F.J. Litterst, K.D. Becker, Enhanced magnetisation in nanocrystalline high-energy milled  $\text{MgFe}_2\text{O}_4$ . *Scr. Mater.* **48**, 961–966 (2003)
30. I. Bergmann, V. Šepelák, K.D. Becker, Preparation of nanoscale  $\text{MgFe}_2\text{O}_4$  via non-conventional mechanochemical route. *Sol. State Ion.* **177**, 1865–1868 (2006)
31. J. Jadhav, S. Biswas, A.K. Yadav, S.N. Jha, D. Bhattacharyya, Structural and magnetic properties of nanocrystalline Ni–Zn ferrites: in the context of cationic distribution. *J. Alloys Compd.* **696**, 28–41 (2017)
32. M.A. Gabal, Y.M. Al Angari, Effect of diamagnetic substitution on the structural, magnetic and electrical properties of  $\text{NiFe}_2\text{O}_4$ . *Mater. Chem. Phys.* **115**, 578–584 (2009)
33. MdS Hossain, S.M. Hoque, S.I. Liba, S. Choudhury, Effect of synthesis methods and a comparative study of structural and magnetic properties of zinc ferrite. *AIP Adv.* **7**, 105321 (2017)
34. M.K. Anupama, N. Srinatha, S. Matteppanavar, B. Angadi, B. Sahoo, B. Rudraswamy, Effect of Zn substitution on the structural and magnetic properties of nanocrystalline  $\text{NiFe}_2\text{O}_4$  ferrites. *Ceram. Int.* **44**, 4946–4954 (2018)
35. J. Curiale, M. Granada, H.E. Troiani, R.D. Sanchez, A.G. Leyva, P. Levy, K. Samwer, Magnetic dead layer in ferromagnetic manganese nanoparticles. *Appl. Phys. Lett.* **95**, 043106 (2009)
36. J. Chappert, R.B. Frankel, Mössbauer study of ferrimagnetic ordering in nickel ferrite and chromium-substituted nickel ferrite. *Phys. Rev. Lett.* **19**, 570–572 (1967)
37. T.M. Clark, B.J. Evans, Enhanced magnetization and cation distributions in nanocrystalline  $\text{ZnFe}_2\text{O}_4$ : a conversion electron Mossbauer spectroscopic investigation. *IEEE Trans. Mag.* **33**, 3745 (1997)
38. A.E. Berkowitz, R.H. Kodama, S.A. Makhlool, F.T. Parker, F.E. Spada, E.J. McNiff Jr., S. Foner, Anomalous properties of magnetic nanoparticles. *J. Magn. Magn. Mater.* **196–197**, 591–594 (1999)

39. J.P. Chen, C.M. Sorensen, K.J. Klabunde, G.C. Hadjipanayis, E. Devlin, A. Kostikas, Size-dependent magnetic properties of  $\text{MnFe}_2\text{O}_4$  fine particles synthesized by coprecipitation. *Phys. Rev. B: Condens. Matter* **54**, 9288–9296 (1996)
40. S. Verma, P.A. Joy, Magnetic properties of superparamagnetic lithium ferrite nanoparticles. *J. Appl. Phys.* **98**, 124312 (2005)
41. B.K. Banerjee, On a generalized approach to first and second order magnetic transitions. *Phys. Lett.* **12**, 16–17 (1964)
42. J. Mira, J. Rivas, F. Rivadulla, C. Vázquez-Vázquez, M.A. López-Quintela, Change from first- to second-order magnetic phase transition in  $\text{La}_{2/3}(\text{Ca}, \text{Sr})_{1/3}\text{MnO}_3$  perovskites. *Phys. Rev. B* **60**, 2998 (1999)
43. H. Saito, T. Yokoyama, K. Fukamichi, Itinerant-electron metamagnetism and the onset of ferromagnetism in Laves phase  $\text{Lu}(\text{Co}_{1-x}\text{Ga}_x)_2$  compounds. *J. Phys.: Condens. Matter* **9**, 9333 (1997)
44. V.K. Pecharsky, K.A. Gschneidner Jr., Magnetocaloric effect and magnetic refrigeration. *J. Magn. Magn. Mater.* **200**, 44–56 (1999)
45. A. Verma, T.C. Goel, R.G. Mendiratta, P. Kishan, Magnetic properties of nickel–zinc ferrites prepared by the citrate precursor method. *J. Magn. Magn. Mater.* **208**, 13–19 (2000)
46. R. Felhi, H. Omrani, M. Koubaa, W. Cheikhrouhou Koubaa, A. Cheikhrouhou, Enhancement of magnetocaloric effect around room temperature in  $\text{Zn}_{0.7}\text{Ni}_{0.3-x}\text{Cu}_x\text{Fe}_2\text{O}_4$  ( $0 \leq x \leq 0.2$ ) spinel ferrites. *J. Alloys Compd.* **758**, 237 (2018)
47. R. Thljaoui, W. Boujelben, M. Pekala, K. Pekala, J.F. Fagnard, P. Vanderbemden, M. Donten, A. Cheikhrouhou, Magnetocaloric effect of monovalent K doped manganites  $\text{Pr}_{0.6}\text{Sr}_{0.4-x}\text{K}_x\text{MnO}_3$  ( $x=0$  to 0.2). *J. Magn. Magn. Mater.* **352**, 6–12 (2014)

**Publisher's Note** Springer Nature remains neutral with regard to jurisdictional claims in published maps and institutional affiliations.